Mechanically Optimized Design and Validation of an Outdoor Automated Guided Vehicle

Muhammad Afzal Khan [1]*, Anas Ahmad Abbasi [2] and Nabeel Ahmed [2,]

Affiliation: [1]*Institute, Mechanical, Hohai University, Nanjing, Jiangsu, China; l*x20220519004@hhu.edu.cn

* Correspondence: afzal.khan.ak1066@gmail.com, abbasianasahmad@gmail.com

Abstract: Automated guided vehicles (AGVs) improve productivity by automating material transport; however, outdoor environments present challenges such as variable friction, uneven terrain, and dynamic loads. Traditional AGV designs lack robustness for outdoor use, requiring a mechanically optimized solution. This study presents the mechanical design and performance analysis of a dual-motor outdoor AGV, emphasizing compactness ≤70 kg, lightweight structure, and reliable operation across diverse surfaces. The design addresses frictional resistance, drivetrain selection, and structural integrity under dynamic loading. Using CAD tools, the AGV was modeled, and key components were validated through analytical calculations focusing on torque transmission, gear reduction, and synchronization. The total resistance of 1260.83 N was determined by summing the frictional resistance of 1200 N, the acceleration of 60 N, and negligible air resistance. Two D80-02430B5-E DC servo motors (0.75 kW, 2.39 Nm) were employed in a dual-drive configuration, each paired with a two-stage planetary gear reducer (PLE-080, 40:1) for torque amplification. An 8 M-type synchronous belt (40 mm width) with automatic tensioning ensured synchronized wheel motion. Shaft diameters 22–27 mm and A-type flat key connections were verified through stress analysis to meet 45-steel limits σ ≤ 60 MPa. The AGV achieved a total driving force of 1260 N with all stresses 20.5–81.8 MPa within allowable limits. The proposed design demonstrates suitability for outdoor logistics, flexible manufacturing, and warehouse automation, offering adaptability, compactness, and cost-effective operation. Future work may integrate advanced navigation and perception systems to enhance autonomous performance.

Keywords: Computer-Aided Design; Planetary Gear Trains; Power Transmission; Belt Drives; Structural Optimization; Mechanical Design.

Citation:

1. Introduction

Material flow is a key part of industrial logistics. Instead of traditional conveyors, many systems now use Automated Guided Vehicle (AGV)-based material handling for flexibility and automation. AGVs are essential in Flexible Manufacturing Systems (FMS) as they navigate tight spaces and reduce costs [1]. Though AGV technology has existed for decades, originally known as driverless vehicles, modern advancements have made them more capable and widely used [2,3]. Powered by electric motors and guided by control systems, AGVs require a well-designed structure, an appropriate power-to-load ratio, and efficient sensor integration. This project aims to design an AGV structure incorporating all these factors for efficient industrial use [4].

AGV technology has evolved significantly over the past fifty years with advancements in electronic and control technologies. Today, AGVs are widely used in industry to automate various tasks, enhancing manufacturing productivity

and efficiency by operating without direct human supervision [5,6]. These vehicles are primarily powered by electric motors connected through shafts to their wheels, requiring precise control systems to enable accurate long-distance navigation. The balance between the total load capacity of an AGV and the power supplied by its motor is critical for effective operation. Moreover, the design of the control system and the careful selection of sensors contribute greatly to the AGV's flexibility and functional capabilities in modern industrial settings [7,8].

In single-load AGV systems, each vehicle is assigned individual tasks to pick up and transport loads from one station to another without carrying additional loads [9]. The primary operational focus lies in assigning unloaded vehicles effectively to optimize maneuvering and prevent interference with other concurrent vehicle tasks. This approach minimizes load stress and simplifies scheduling since each vehicle handles one load at a time. Techniques such as task prioritization, efficient task assignment algorithms, and route optimization are used to improve system performance and reduce idle vehicle movements [10,11].

Multiple-load AGV systems involve more complex operations where AGVs carry multiple loads simultaneously, including additional loads picked up from intermediate stations [12]. This increases throughput and flexibility of material handling systems, especially in environments like FMS that require adaptable logistics solutions. However, the multi-load nature introduces significant challenges in scheduling and control, requiring advanced planning, dispatch, and task assignment algorithms to efficiently manage dynamic tasks and vehicle distribution [13,14].

Therefore, this study focuses on the mechanical design of a compact outdoor AGV that combines these key factors to enhance performance in low-weight, high-efficiency applications. The main objective is to utilize CAD tools for the mechanical design, component selection, and performance validation based on given parameters, ultimately developing a robust outdoor AGV capable of reliable operation across varied surfaces.

2. Literature Review

The development of Automated Guided Vehicles (AGVs) has evolved significantly since their introduction as unit load vehicles in the 1970s. These early systems served multiple functions ranging from simple transport platforms to components integrated with broader control and information systems [15]. Over time, AGVs have transformed from basic mail-handling units to sophisticated machines equipped with advanced sensors, LiDAR, and AI-based navigation modules, offering increased adaptability in modern manufacturing and logistics environments. This evolution is driven by the need for enhanced perception, precise navigation, and intelligent decision-making in increasingly complex operational settings [16,17].

Recent years have witnessed a growing focus on outdoor AGV applications, driven by the expansion of smart warehousing and last-mile logistics [18,19]. Traditionally, AGVs were primarily used for tasks such as moving pallets, containers, or assembly line processes in warehouses and manufacturing facilities. However, outdoor environments pose significant challenges compared to controlled indoor settings due to variable terrain and environmental factors [20,21]. While much literature focuses on indoor AGVs, there is increasing recognition of the distinct mechanical challenges presented by outdoor operation [22]. The mechanical system of an AGV, including components such as the chassis, motors, gears, and wheels, is critical to its overall performance [23].

Another key area of innovation involves drive systems and transmission mechanisms, which are crucial for the performance and durability of AGVs—especially in demanding outdoor environments. The selection of appropriate drive systems and transmission methods directly impacts an AGV's ability to handle varying loads and terrains [24,25].

Harmonic drives are known for their precision and compact design, making them suitable for applications requiring high accuracy and minimal backlash [26]. However, a significant limitation of harmonic drives is their reduced durability when subjected to shock loads, making them less ideal for heavy-duty outdoor applications where sudden impacts or uneven terrain introduce significant stress [27]. Research has also highlighted challenges in predictive wear modeling of harmonic reducers, emphasizing limitations under strenuous mobile platform conditions [28].

In contrast, planetary gear reducers are a more robust and common choice for AGVs, particularly for heavy-duty mobile platforms. They are favored for their compact size and ability to handle high torque, making them well-suited for applications where space is limited but power transmission is critical [29]. Their design allows for even load distribution among multiple gears, contributing to durability and reliability under challenging conditions. Studies have verified their effectiveness in various non-stationary scenarios through experimental results from planetary gearbox datasets [30,31].

The AGV design in this project incorporates novel structural and functional enhancements to optimize outdoor performance, specifically featuring a dual-motor symmetric differential drive [32]. This system improves traction and stability on irregular surfaces by enabling each motor to power both front and rear wheels on its respective side through a synchronous belt transmission. While similar approaches exist, few have applied this configuration in a compact AGV under 70 kg, maintaining a balanced torque profile across all wheels. Additionally, the use of an automatic belt tensioning system addresses belt slippage, a common issue in dust-prone outdoor environments [33,34].

Therefore, despite utilizing standard mechanical components such as planetary gearboxes and rolling bearings, this AGV design makes a unique contribution through the integration of lightweight symmetry, dual-axis control, and autonomous belt management—collectively enhancing performance and reliability for compact outdoor AGVs.

3. Mechanical Design

3.1. AGV Model

The AGV comprises several parts, including the body frame, drive mechanisms, battery, rotor, and control system. It measures 1000 mm in length 680 mm in width and 250 mm in height. The left and right wheels are spaced 680 mm apart while the front and rear wheels are 596 mm apart. The drive mechanisms are symmetrically positioned at the center and connected to the wheels. To ensure balance, the control module and battery (power supply) are centrally mounted. During operation, the power supply activates the transmission and control module which manages the drive mechanism for starting to stop, and steering. This thesis emphasizes the design of the structure and transmission system excluding the battery and control module design.

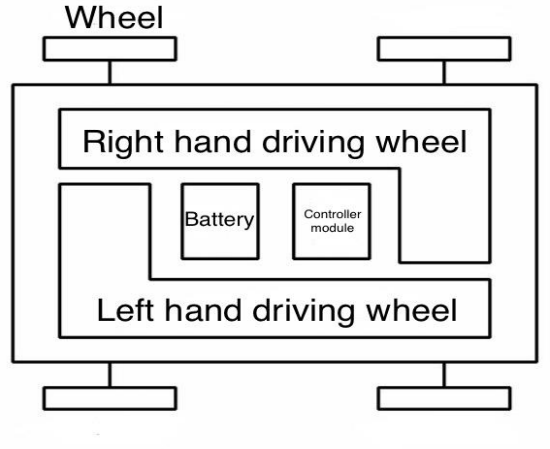

Figure 1. AGV overall layout

Figure 2. Mechanical design of outdoor AGV

3.2. Identification of the Drive Program

This project primarily designs a non-steering mechanism differential AGV structure, focusing on the transmission mechanism [25]. The AGV achieves steering by the difference in speed between the left and right wheels, requiring both sides to have equal speed during straight motion. All four wheels are drive wheels. One motor control two wheels on the same side, reducing body size and weight. The motor connects directly to the

gearbox to enhance torque and transmits power through a coupling to the rear axle. The motion is transferred to the other wheel on the same side via a synchronous belt with a 1:1 ratio, maintaining equal wheel speeds. The left and right drive mechanisms are symmetrically installed at the center of the body, ensuring smooth and stable movement. During operation, each motor powers its side independently, and steering is achieved by adjusting the speed difference between the motors [25]. The primary drive plan is shown in Figure 2.

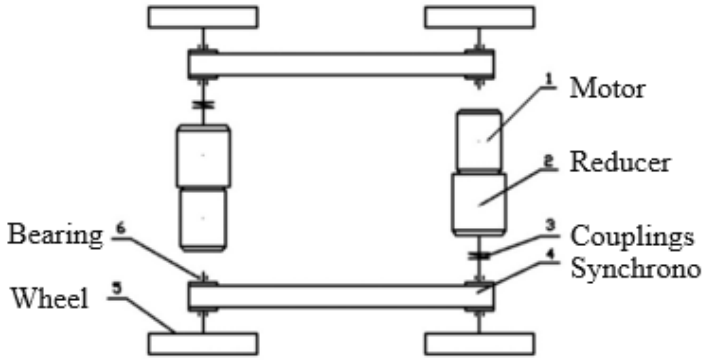

Figure 3. Background on AGV drive mechanism

3.3. Electric Motors

For an outdoor automated guided vehicle (AGV) a battery-powered DC motor is used to accommodate diverse operating conditions. In comparing servo motors and stepper motors, servo motors are often preferred [26]. Servo motors offer enhanced control accuracy stable torque at rated speeds effective overload handling and rapid response making them ideal for uneven outdoor terrain [27]. Consequently, DC servo motors are selected for this design to ensure reliable performance in outdoor environments [28]. Therefore, DC servo motors are selected for this design.

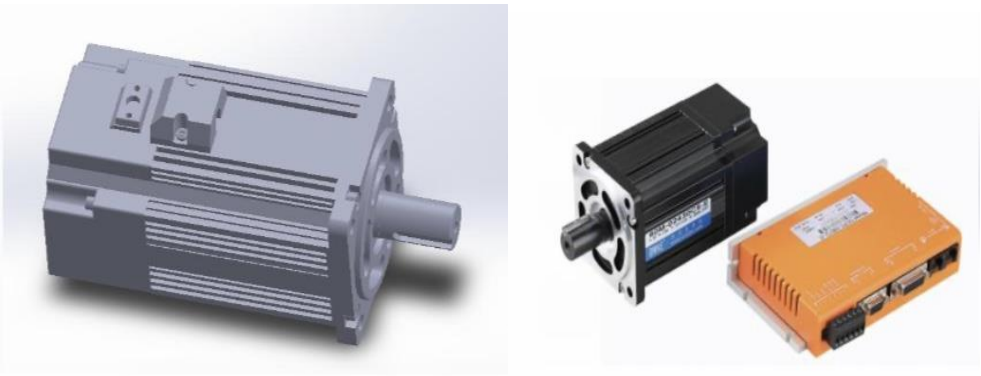

Figure 4. Motor model diagram

The power provided by the motor is 0.378 kW, and the required torque is 1.575 N.m. Considering power and torque requirements, the motor D80-02430B5-E from Demarco is selected. It is rated at 0.75 kW and delivers 2.39 Nm torque at 3000 rpm under standard conditions and weighs approximately 2.4 kg.

3.4. Gearbox

Gearboxes like cylindrical, Worm gear reducers are characterized by their cylindrical gears with a spiral thread that drives worm gears [29]. Worm reducers are cheap and self-locking but bulky and inefficient, unsuitable for compact AGVs. and Harmonic gear reducers are noted for their precision and compact design. Harmonic reducers are precise and compact but lack durability and shock resistance [30], making them unfit for outdoor AGVs. Cylindrical gearboxes are fundamental components in various mechanical systems, responsible for changing speed and direction [31]. Cylindrical reducers are simple but too large for small AGVs.

So, none of these are chosen for this design.

Planetary gear reducers are widely used in power transmission due to their compact size, light weight, and ability to handle high torque [32]. However, the torque of output is low but adequate to meet the operating needs of the AGV.

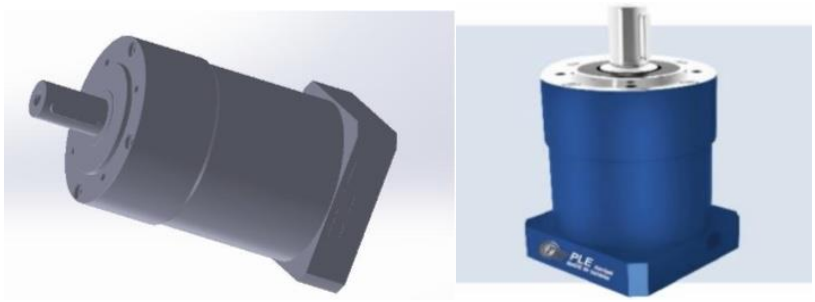

Figure 5. Planetary gear reducer model diagram

Considering the AGV working environment and gearbox characteristics, the planetary gear reducer is finally selected as the AGV decelerator, as shown in Figure 4. Select a PLE-080 type reducer with a deceleration ratio of 40, a rated output torque of 110 Nm and a weight of 3.2 kg.

3.5. Couplings

Couplings transmit power between shafts, useful when long shafts are not practical. Rigid couplings are simple but inflexible, while flexible ones absorb misalignment and vibration [33]. This outdoor AGV uses an elastic pin tooth coupling between the reducer and rear axle to reduce shock, vibration, and noise [34].

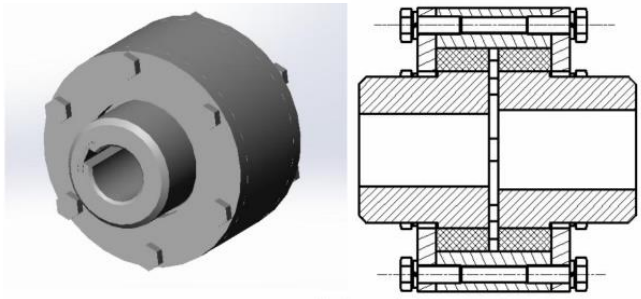

Figure 6. Elastic column pin tooth coupling

3.6. Key

In practical applications, key type and size are chosen based on working conditions, with strength checks if needed. On the rear axle, key connections are used at the shaft wheel, shaft-pulley, and shaft-coupling. This design uses A-type flat keys. According to the mechanical book.

shaft diameter at the connection with the AGV wheel is 22mm.

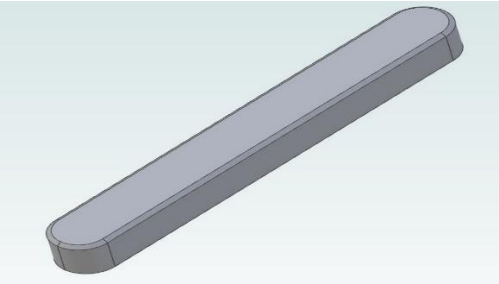

Figure 7. A-type flat key

The size of the selected key.

Width b = 8mm,

Height h = 7mm,

According to the length of the connection between the shaft and the wheel.

Select the key length L = 20mm

(1) The shaft diameter at the synchronous pulley is 27mm,
The cross-section size of the selected key.

Width b = 8mm,

Height h = 7mm,

Considering the length of the keyway on the pulley.

The key length is L = 40mm.

(2) The shaft diameter at the connection with the coupling is 22mm,
The cross-section size of the selected key is.

Width b = 8mm,

Height h = 7mm,

According to the coupling model, the key length L = 28mm

4. Mechanical Analysis and Design Verification

4.1. Calculation of Driving Force

For frequent travel, the AGV must overcome all resistances, so the required driving force (F_T) equals the total resistance [35]. As an outdoor AGV, it faces more complex forces than indoor ones, from.

This formula can be used to measure the driving force needed during AGV operation.

$$F_T = F_f + F_j + F_w \quad (1)$$

4.2. Rolling and Sliding Friction Analysis

AGV stress varies by movement. Rolling friction dominates at 8 km/h in straight motion, while sliding friction takes over during 2 km/h steering. Since steering has higher resistance, it is used for power calculations.

The formula calculates the rolling friction F_{f1} during the AGV's straight-line movement.

$$F_{f1} = f_{Fn} \quad (2)$$

Since the AGV operates outdoors, it may run on asphalt, cement, or gravel roads. Gravel has the highest friction. Using a friction coefficient f=0.015 and a total mass m = 120 kg (AGV + load), the rolling friction F_{f1} is calculated for the worst-case (gravel) condition.

$$F_n = mg \quad (3)$$

$$g = 10\ N/kg,$$

$$F_n = mg$$

$$F_n = 120 \times 10 = 1200$$

$$F_n = 1200$$

So now we have to put f and F_n In equation (2)

$$F_{f1} = 0.015 \times 1200$$

$$F_{f1} = 18N$$

The friction steering F_{f2} can be calculated by equation (2-4)

$$F_{f2} = \mu F_n \quad (4)$$

μ is the sliding coefficient of friction

On newly repaired asphalt, the AGV faces a high sliding friction coefficient of up to 1.0 due to natural rubber contact. Using this, the normal force μ=1.0. So, in equation (3), $F_n = 1200$

Now μ and F_N we will put in equation (4)

$$F_{f2} = \mu F_n$$

$$F_{f2} = 1.0 \times 1200$$

$$F_{f2} = 1200\ N$$

In summary, although the steering speed is lower, the friction is much higher, about sixty-seven times more than during straight movement. So, for design, the steering phase is used with friction $F_{f2} = 120N$ at 2 km/h.

4.5. Accelerated Resistance Calculation

To reach its working speed, the AGV must overcome acceleration resistance. Faster acceleration improves efficiency and flexibility but may reduce safety [37]. So, the max acceleration is limited to α = 0.5m/s2 [36].

$$F_j = ma \qquad (5)$$

$$F_j = 120 \times 0.5$$

$$F_j = 60\ N$$

4.6. Air Resistance Calculation

The air resistance, or aerodynamic drag, is a force that opposes the motion of the Automated Guided Vehicle (AGV) through the air. This force can be calculated using a standard formula incorporating air density, the drag coefficient, the vehicle's frontal area, and its speed [37].

$$F_w = \frac{1}{2} CdA\rho u^2 \qquad (6)$$

ρ=1.225kg/m3 (air density)

Cd=1.1 (drag coefficient)

$A=0.25\ m^2$ (estimated frontal area of the AGV 0.5 m width × 0.5 m height)

$v=3.68km/h=2.22m/s$ (speed in m/s)

$$F_w = \frac{1}{2}\ 1.1 \times 0.25 \times 1.225 \times (2.2)^2 = 0.83\ N$$

So, we calculated frictional resistance, acceleration resistance, and air resistance.

Put in equation (1)

$$F_t\ = F_{f2} + F_j\ + F_w$$

$$F_t\ =\ 1200\ +\ 60\ +\ 0.83$$

$$F_t = 1260.83\ N$$

4.7. Power and Torque Requirements

The AGV must generate enough power to overcome resistance and reach its required speed [38]. This total power is calculated using the formula.

$$P_w\ =\ F_t v \qquad (7)$$

V is AGV running speed in m/s,

$$V = 2km/h = \frac{5}{9}\ m/s$$

$$Pw\ =\ 1260 \times \frac{5}{9}$$

$Pw = 700W = 0.7\ kW.$

The calculated power is the total power needed for the AGV's operation. Because the differential AGV without a steering mechanism has four wheels, the power required for each wheel is the same.

$$P_{w1} = \frac{P_w}{4}$$

$$P_{w1} = \frac{0.7}{4}$$

$$P_{w1} = 0.175\ kW$$

The AGV drive system uses two motors, each powering one side (two wheels). Power is delivered through a gearbox and a synchronous belt. Due to transmission losses, the actual motor power P_d must be adjusted [39]. as shown in equation (8).

$$P_d = \frac{P_{w1}}{\eta_1} + \frac{P_{w1}}{\eta_2} \quad (8)$$

A second-stage planetary reducer is pre-selected to ensure a safety margin. The gearbox has an efficiency of 0.94, and the belt drive efficiency is 0.97.

So, there is.

$\eta_1 = 0.97 \times 0.94 = 0.91\%,$

$\eta_2 = 0.94\%$

Now put the value in equation (8)

$Pd = 0.384\ kW$

Besides meeting power needs, the AGV must generate enough torque to overcome resistance. Since one motor drives both front and rear wheels on the same side, the gearbox torque N_t must cover both. It has calculated using equations (9).

$$N_t = \frac{F_t}{4} \times \frac{D}{2} \times 2 \quad (9)$$

According to some AGV product descriptions, the wheel diameter D = 200mm,

Now we have to put in equation (9)

$$N_t = \frac{F_t}{4} \times \frac{D}{2} \times 2$$

$$N_t = \frac{1260}{4} \times \frac{200}{2} \times 2 = 63N.m$$

The gearbox gets its output torque from the motor, so the motor must deliver enough torque to meet this need. The required motor torque N_d It is calculated using formula (10), based on the reducer's torque demand.

$$N_d = \frac{Nt}{i} \quad (10)$$

where the deceleration ratio is assumed to be 40.

Now we have to put in equation (10),

$$N_d = \frac{Nt}{i}$$

$$N_d = \frac{63}{40} = 1.575\ N.m$$

4.8. Synchronous belt drive

This design uses a 1:1 synchronous belt to drive both wheels on one side of the AGV with a single motor. To keep the AGV compact, the belt replaces gears and is positioned at the low-speed end. It handles short-term loads during steering and offers precise, efficient, and smooth transmission with strong impact resistance. Synchronous belts are commonly used in various transmission systems due to their positive engagement and efficient power transfer capabilities [40].

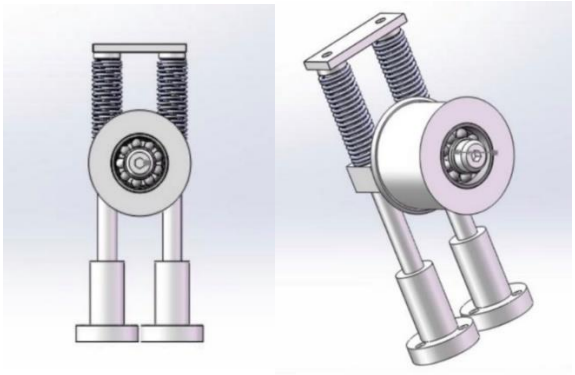

Figure 8. Automatic tensioning device of synchronous belt

4.9. Belt tensioning device for synchronous belt

In power transmission systems, rubber synchronous belts can deform under load, leading to reduced efficiency and increased wear. To counteract this, an automatic tensioning device is employed, replacing manual tension checks [41]. Due to limited AGV space a smooth tensioning wheel is placed outside the belt, centered between equal-sized pulleys. The system includes vertical shafts, a slider, a tensioning wheel, and springs. The slider is fixed with plug screws and rotates freely on bearings. Shafts pass through to prevent twisting. A spring-loaded shaft cover keeps constant pressure and with the help of gravity, maintains proper belt tension.

4.10. Wheel design and synchronous belt drive system

The arc tooth synchronization band with a smaller root stress set is chosen due to the high strength force in the AGV steering process in this design. The method of design obtained from the book Mechanical Design.

The power Pd is designed (11). As a basis for the selection of wheel rotation by the formula

$$P_d = K_A P \tag{11}$$

P is the power of the wheel transfer in "kW."

K is the condition factor. from (Mechanical Design Book)

Take $K_A = 1.7$

Calculated part 2.3, where $P=0.175\ kW$

$P_d = 1.7 \times 0.175 = 0.2975\ kW$

Synchronized band speed is wheel speed, and the band speed is synchronous. N_t

$$n_t = \frac{v}{2\pi r} \tag{12}$$

v is rear-wheel line speed, and AGV travel speed is in *"m/s."*

r is wheel radius, unit is *"m."*

Substitute 2.4 with partially calculated data

$$n_t = \frac{v}{2\pi r} = \frac{20/0.6}{2\pi \times 0.1} = 53r/min$$

Determination of the number of teeth with wheel teeth and the diameter of the knot circle

Use the belt wheel selection table; choose an 8 M-type synchronous belt wheel.

The sync hone belt pitch $p_b = 8\ mm$

Depending on the Size of the AGV, select $z_1 = 26$

You can then get the knot diameter d_1 by the lower formula.

$$d_1 = p_b z_1 / \pi \tag{13}$$

Z_1 number of main-belt teeth

$$d1 = \frac{8 \times 26}{\pi} = 66.21mm$$

Because the transmission ratio is 1:1, the two-strap teeth are the same as the knot circle radius and other parameters.

from the number of teeth on the wheel, $z_2 = 26$

Knot diameter $d_2 = 66.21mm$

Synchronization with band length determination and tooth numbers.

Based on the size of the car, the center distance is $a_o = 600mm$

Calculate the length of the band's section based on the formula (14).

$$L_{op} = 2\times a_o \frac{\pi}{2}(d_2+d_1)+\frac{(d_2-d_1)^2}{4a_o} \quad (14)$$

$$L_{op} = 2\times 600 \frac{\pi}{2}(66.21+66.21)+\frac{(66.21-66.21)^2}{4\times 600} = 1408mm$$

According to the mechanical design book, take the standard section length of the arc tooth band. $L_p = 1400$ *mm.*

Number of teeth $z_b = 175$

The real center distance will be changed based on the formula (15).

$$a = a_o + \frac{L_p - L_{0p}}{2} \quad (15)$$

$$a = 600 + \frac{1400-1408}{2} = 596mm$$

Due to the completion of the two-belt wheel in the synchronous belt drive, all the same, then the number of rodents on the wheel is $z_m = 13$

4.11. Determination of bandwidth

After determining the band wheel parameters, the synchronous bandwidth b_s can be calculated by the formula.

$$b_s \geq b_{so}\sqrt[1.14]{\frac{P_d}{K_L K_z P_0}} \quad (16)$$

b_{so} is the baseline bandwidth, in *"mm."*

$b_{so} = 20mm$

K_L a long coefficient for arc teeth =1.1

P_0 is the baseline power rating for the synchronous band, in *"kW"*

P_0= 0.1325 kW

K_z The long coefficient of the arc tooth band = 1

$b_s \geq 20\sqrt[1.14]{\frac{0.2975}{1.1\times1\times0.1325}} = 37.$

According to the Mechanical Design textbook, take the standard value $b_s = 40mm$.

The force acting on the axle of a pulley is calculated by the formula (17)

$$F_r = K_F \frac{P_d}{V_d} \times 1500 \quad (17)$$

K_F is the vector sum correction coefficient = 1

V_d Is the velocity of the belt, in *"m/s"*

$V_d = \frac{\pi d_1 n_t}{60\times1000} = \frac{\pi\times66.21\times53}{6000} = 0.184m/s$

Now put values in equation (17)

$F_r = 1\times\frac{0.2975}{0.184}\times1500$

F_r = 2438N

4.12. Pulley check

The sync belt must fulfill the conditions shown in the formula (18) for it to work properly.

$$P_d > P_s \times K_m \times K_b \quad (18)$$

According to the Mechanical Design Textbook,

P_s Is the base drive capacity in *"kW"*

P_s = 0.5kw

K_m The meshing compensation factor =1

K_b The width compensation factor = 0.63

$P_s \times K_m \times K_b$

$0.63 \times 1 \times 0.63 = 0.315kw > 0.2975kW$

So, the synchronous belt is correctly chosen.

4.13. Preliminary design of drive shaft diameter

During AGV operation, torque is transmitted to the rear wheel via a shaft connected to the reducer, while power is transferred to the front wheel through a synchronous belt on the shaft. The minimum diameter of the drive shaft plays a crucial role in determining the design and selection of other components. Therefore, the minimum diameter of the rear-wheel drive shaft is first estimated, followed by its design, which then influences the design of the subsequent parts [43].

Since the layout of the parts on the shaft and its specific force condition have not yet been determined, the minimum diameter d_{min}Is are initially estimated here based on the torque of the shaft.

The shaft neck range can be calculated by formula (19).

$$d \geq \sqrt[3]{\frac{9.55\times10^6 P}{0.2[\tau]n}} = \sqrt[3]{\frac{T}{0.2[\tau]}} \quad (19)$$

Calculated from part 2.3 $t = 63000N{\cdot}mm$

If the shaft material is 45 steels, then $[\tau] = 40MPa$

$$d \geq \sqrt[3]{\frac{63000}{0.2\times40}} = 19.9mm$$

$d \geq 19.9mm$

To keep the shaft strong enough

The minimum diameter of the shaft is initially determined as $d_{min} = 22mm$

4.14. Structure of the rear axle

The differential AGV has four shafts two identical rear axles connected to motors and two identical front axles. The rear axle, linked to the reducer, is designed based on the layout of components. From left to right, it holds the wheel, bearing, pulley, another bearing, and coupling [44]. Parts are secured both axially and circumferentially using keys, shoulders, oil baffles, and end covers. The right end of the shaft is fixed with a key and coupling, which also delivers power [44].

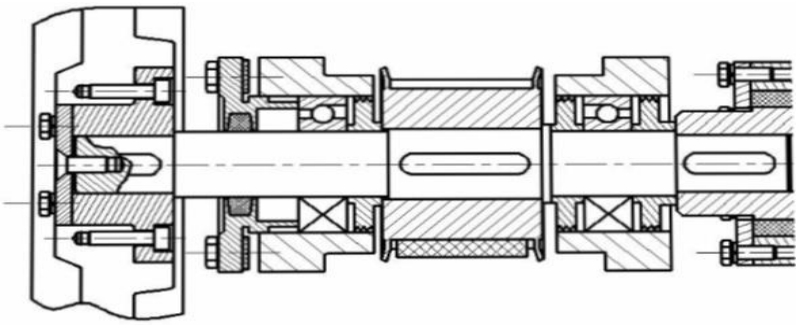

Figure 9. Rear axle structure

4.15. Structure of the front axle

In the AGV, power reaches the front axle through the reducer, coupling, and belt, then drives the front wheel directly [45]. Both axles share a similar layout with wheels, bearings, and pulleys. Unlike the rear axle, the front axle does not connect to a reducer, so it lacks a coupling on the right end. Bearings are fixed with shaft shoulders and end covers, and a felt ring prevents dust from entering [44].

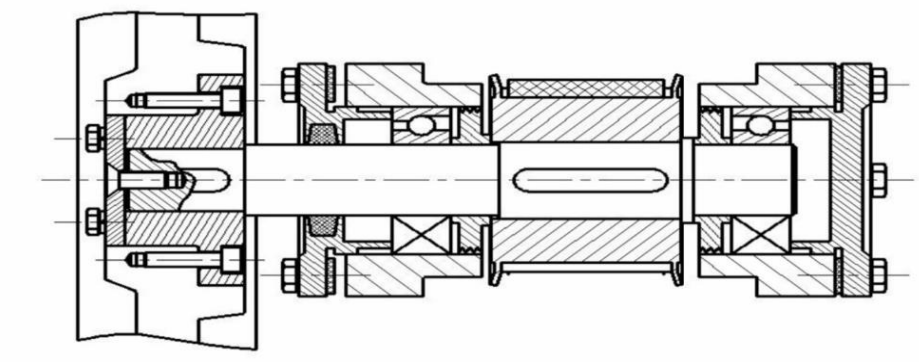

Figure 9. Front Axle Structure

5. Results

5.1. Rear axle strength and stress verification

During AGV operation, the shaft experiences both bending and torsion forces. After determining the size and structure of the shaft, it is essential to check the strength of certain sections to ensure the safety and reliability of the AGV's operation. This part will refer to the "Mechanical Design" textbook [15] for a detailed stress analysis and strength verification of the rear axle.

The 3D stress distribution (Figure 16) shows how the shaft behaves under a 63 Nm torque load. The shaft was fixed at the left end, and the torque was applied at the right. As expected, stress concentration increases along the shaft length, particularly near the central region and the keyway slots where geometry transitions occur. The maximum von Mises stress reaches approximately 55 MPa, which remains within the allowable limit for 45 steel (60 MPa), validating the safety of the design under expected working conditions.

5.1.1. Stress diagram of the shaft.

According to the layout of parts on the shaft and the stress of parts on the shaft. The stress diagram of the shaft, as shown in Figure 9, can be obtained.

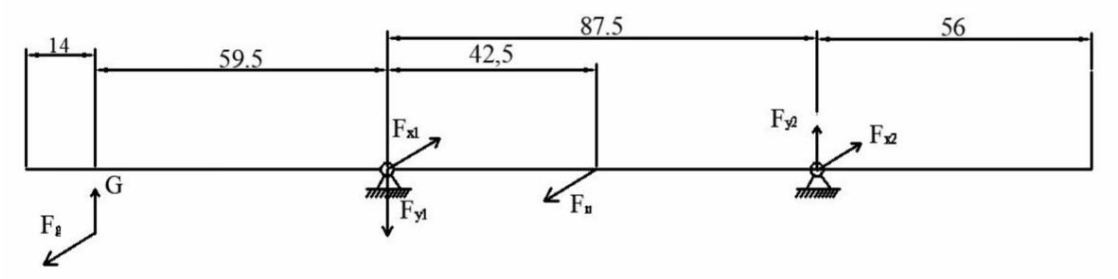

Figure 10. Stress diagram of the rear axle.

Find the force applied on the shaft.

Through motor type selection and calculation of the pulley design part.

GET.

G= 300N

$F_g = 315N$

$F_n = 2438N$

According to the equilibrium conditions of the theoretical mechanical force system, the mechanical equilibrium equations shown in equation (20) can be obtained.

$$\begin{Bmatrix} F_{x1} + F_{y1} = F_g F_n \\ F_{y1} + F_{y2} = G \\ G \times 59.5 = F_{y2} \times 87.5 \\ F_g \times 59.5 + F_{x2} \times 87.5 = F_n \times 42.5 \end{Bmatrix} \quad (20)$$

$F_{x1} = 1783N$

$F_{y1} = 504N$

$F_{x2} = 970N$

$F_{y2} = 204N$

In this verification, two critical sections of the shaft are selected for strength analysis the section where the left bearing is located (defined as section 1) and the section where the pulley is located (defined as section 2).

To calculate the moments at these dangerous sections, the horizontal plane moment M_{xz} and the vertical plane moment M_{yz}Are determined using the formula (21).

$M_1 = F \times I$ *(21)*

Finally, the synthetic bending moment M is calculated by a formula (22).

$$M = \sqrt{{M_{xz}}^2 + {M_{yz}}^2} \quad (22)$$

Were.

F is the force

I is the distance between the point of application and the origin

Substitute the data to obtain Section 1.

$M_{xz1} = 18.7\ N.m$

$M_{yz1} = \ 17.9\ N.m$

$M_1 = \ 25.9\ N.m$

Substitute the data to obtain Section 2.

$M_{xz2} = \ 43.6\ N.m$

$M_{yz2} = = \ 9.2\ N.m$

$M_2 = \ 44.6\ N.m$

5.2. Verification of the front axle

The front and rear axles are rotating shafts in terms of force characteristics. The front axle is primarily influenced by the friction force from the ground to the wheel, the supporting force from the ground to the wheel, the force from the pulley to the axle, and the force applied to the shaft by the bearing. Compared to the rear axle, the front axle experiences simpler forces and is subjected to less load, though the journal in its key part is similar to that of the rear axle.

Since the strength of the rear axle has been thoroughly verified in equation 25 and meets the AGV's requirements, it can be concluded that the front axle, with its simpler stress situation, will also meet the necessary strength requirements for its operation. Therefore, no additional strength check is required for the front axle.

5.3. Bending Moment Diagram

Bending moment diagram between two bearings according to the calculated force and bending, and twisting.

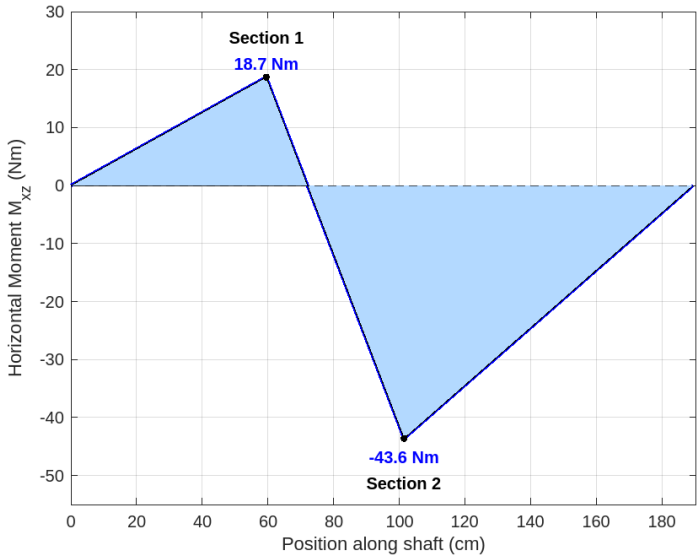

Figure 11. Horizontal bending moment diagram

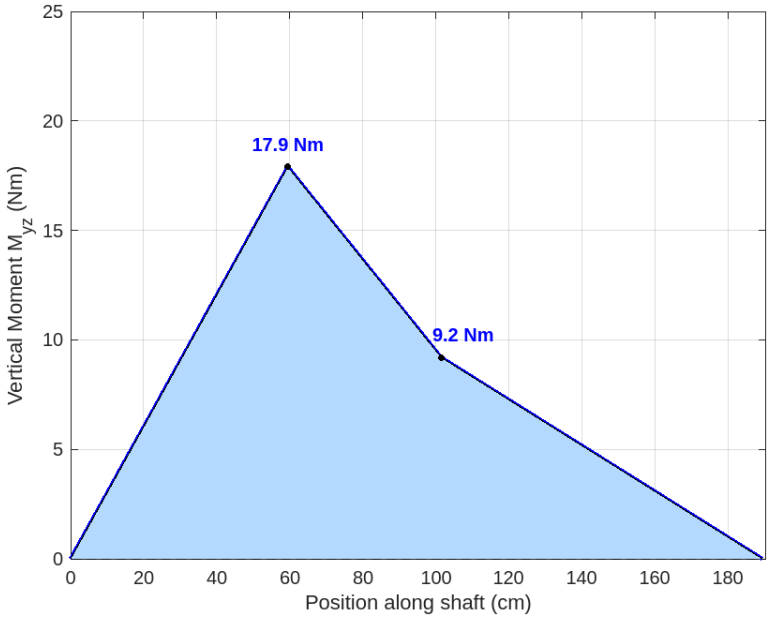

Figure 12. Vertical bending moment diagram

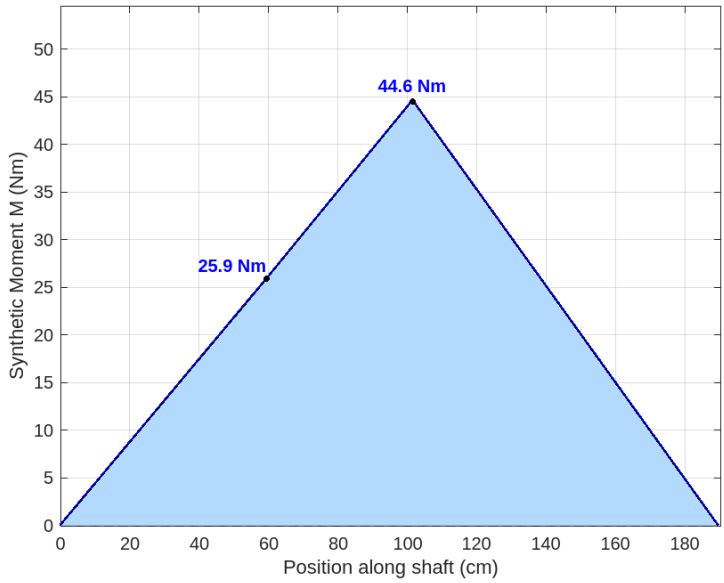

Figure 13. Synthetic bending moment diagram

Fig. 11 shows the horizontal bending moment diagram of the rear axle, where the vertical line represents the wheel position, left end bearing position, pulley position, and right end bearing position. Similarly, Fig. 10 shows the bending moment diagram for the vertical plane, with the vertical line indicating the same positions as in Fig. 14. This diagram illustrates the bending moment generated by the force acting on the shaft in the vertical plane.

The bending moments from both the horizontal and vertical planes are combined using formula (22) to generate the synthetic bending moment diagram, as shown in Figure 13.

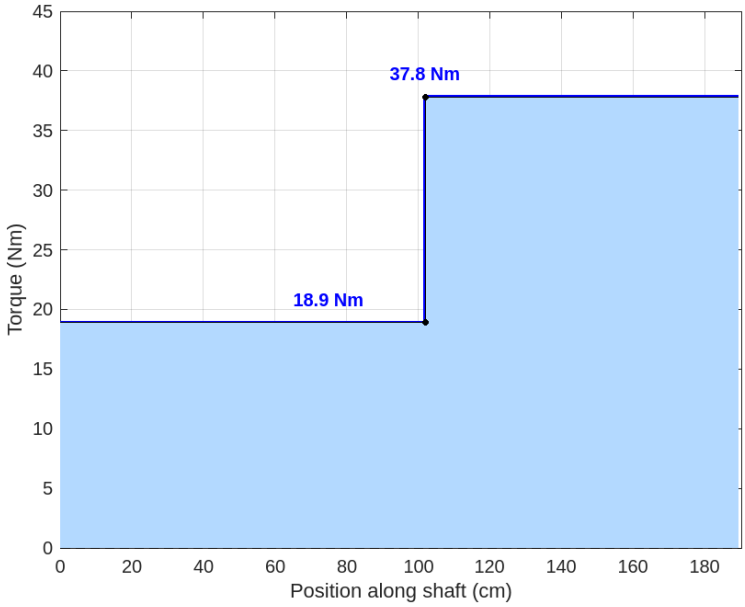

Figure 14. Torque diagram

The moment of the rear axle is different in different axle sections, and its moment can be calculated by the formula (23).

$$T_\alpha = \alpha T \tag{23}$$

Where

α is the reduction coefficient determined according to the torque property and the stress condition of the rear axle.

so $\alpha = 0.6$

T is the torque transmitted by the rear axle, input data.

The torque on the shaft from the wheel to the pulley is $18.9\ Nm$.

The force from the pulley to the coupling is $37.8\ Nm$.

Draw the torque diagram shown in Figure 14 based on the calculations.

Finally, according to formula (24), the equivalent bending moment M_v of the rear axle is obtained.

The equivalent bending moment diagram, as shown in Figure 11-15, is drawn.

$$M_v = \sqrt{{T_1}^2 + (\alpha T)^2} \tag{24}$$

The equivalent bending moment of section 1 is $M_v = \sqrt{{T_1}^2 + (\alpha T)^2}$

$M_v = \sqrt{(25.9)^2 + (18.9)^2} = 32.1\ Nm$

Because the torque has suddenly changed in Section 2, the equivalent bending moment of Section 2 also changes abruptly,

Since the torque has mutated at section 2, the equivalent bending moment at section 2 also mutates.

The equivalent bending moment of section 2 is $M_{v2} = \sqrt{{T_2}^2 + (\alpha T_2)^2}$

$M_{v2} = \sqrt{(25.9)^2 + (18.9)^2} = 48.4\ N.m$

The equivalent bending moment after mutation is *58.5 Nm*.

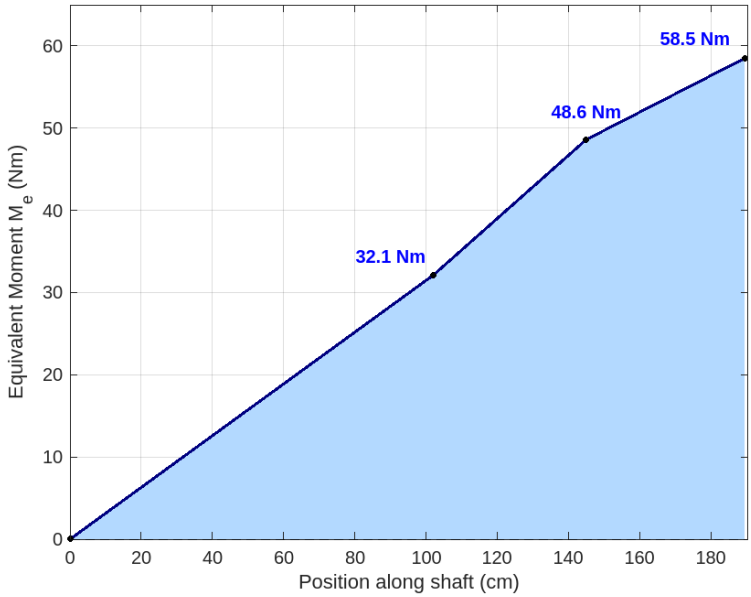

Figure 15. Equivalent bending moment diagram

5.4. Strength of the shaft

According to the bending moment diagram, check the bending and torsional strength of section 1 and section 2.

Section 1

Shaft diameter at the left end bearing d_1 = 25mm

Section 2

Shaft diameter at pulley $d_2 = 27mm$

Calculate the equivalent bending stress σ_v According to equation (25),

It is compared with the allowable bending stress $[\sigma_{-1b}]$

The allowed bending stress is $[\sigma_{-1b}]$ = 60 MPa for 45 steels treated according to the Mechanical Design textbook.

$$\sigma_v = \frac{M_v}{0.1d^3} \times 10^3 \qquad (25)$$

By substituting the data, the equivalent bending stress in Section 1 is $\sigma_{v1} = \frac{M_{v1}}{0.1{d_1}^3} \times 10^3$

$$\sigma_{v1} = \frac{32.04}{0.1\times25^3} \times 10^3 = 20.5Mpa$$

20.5<60, the equivalent bending stress is much smaller than the allowable bending stress, so the axial strength at Section 1 meets the design requirements.

By substituting the data, the equivalent bending stress in Section 2 is $\sigma_{v2} = \frac{M_{v2}}{0.1{d_2}^3} \times 10^3$

$$\sigma_{v2} = \frac{58.64}{0.1 \times 27^3} \times 10^3 = 29.7Mpa$$

20.5<60, the equivalent bending stress is far less than the allowable bending stress, so the axial strength at Section 2 also meets the design requirements.

In summary, the strength of the rear axle meets the requirements.

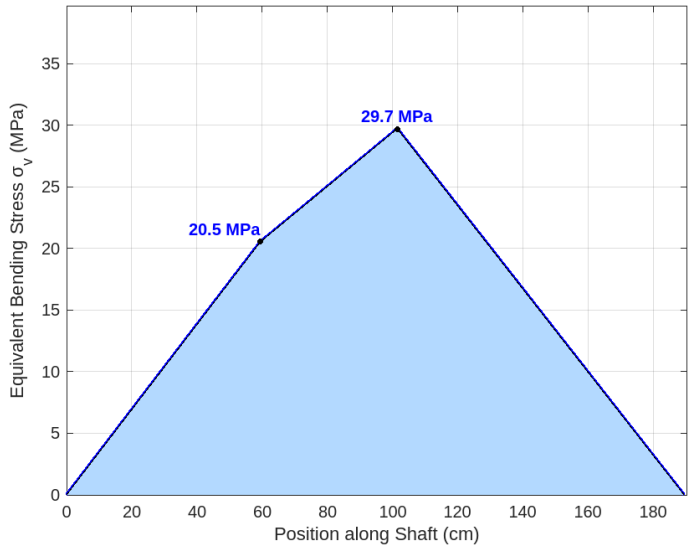

Figure 16. Equivalent bending stress

5.3. Bearing selection and load validation

Bearings are essential for machine performance and are classified by friction type sliding or rolling [45]. Sliding bearings are complex and non-standard, while rolling bearings are standard, efficient, and cost effective [45]. This AGV uses rolling bearings to support the rear axle. Due to side sliding steering and complex road

conditions, the axle experiences axial load, so angular contact ball bearings (7205AGJ, 25 mm inner and 52 mm outer diameter) are chosen for their suitable contact angle.

Figure 10. Angular contact ball bearings

5.3.1 Bearing load analysis and dynamic rating verification

Abnormal vibration or excessive heat during operation indicates potential bearing failure, typically due to fatigue pitting or plastic deformation, which causes surface wear. To ensure reliable AGV operation, it is important to check the bearing. This is done by comparing the required dynamic load with the selected bearing rated load [46]. Since the front axle's stress is similar to the rear axle, the rear axle bearing will be checked for suitability, calculation of equivalent dynamic load.

The equivalent dynamic load of the rolling bearings P1 can be calculated by formula (26)

$$P_1 = f_p(XF_r + YF_a) \tag{26}$$

Fr 、 Fa are the radial load and axial load of the bearing, respectively; X, Y are the radial coefficient and axial coefficient, respectively. F_p It is the load factor. Considering the slip-sliding that occurs during the operation of the AGV, the sliding friction of the single wheel is taken as the axial load.

F_a=300N. At the same time, the AGV is subject to a moderate impact during operation. So F_p = 1.2.

$$F_r = \sqrt{{F_x}^2 + {F_y}^2} \tag{27}$$

Through the calculation in Section 2.6, the horizontal force and vertical force on the bearing are substituted into formula (29),

The radial load of the left-hand bearing is $F_{r1} = \sqrt{{F_x}^2 + {F_y}^2} = \sqrt{1783^2 + 504^2} = 1852.86\ N$

The radial load of the right-hand bearing is $F_{rr} = \sqrt{{F_{x2}}^2 + {F_{y2}}^2} = \sqrt{970^2 + 204^2} = 991.22\ N$

Among them, the force of the left-hand bearing is far greater than that of the right-hand bearing, so only the left-hand bearing is checked.

$$\frac{F_a}{F_r} = \frac{300}{1852.86} = 0.162 < 0.68$$

From the (mechanical design book), $X = 0.41$, $Y = 0.87$.

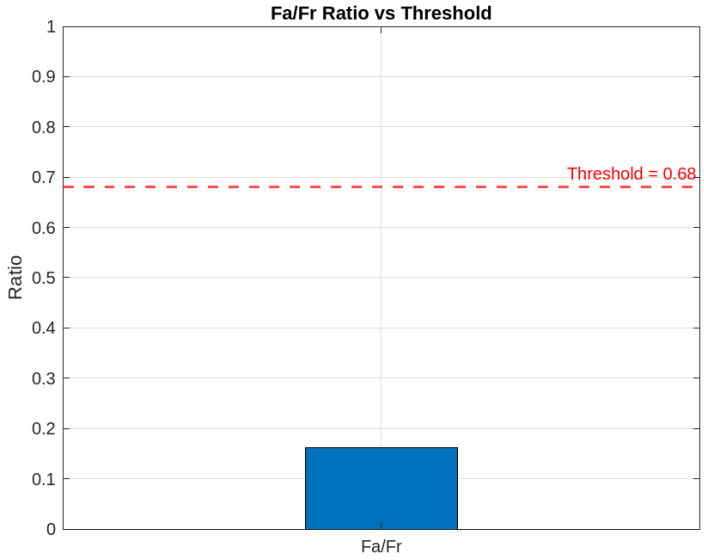

Figure 11. Ratio VS Threshold

The equivalent dynamic load is required by substituting the obtained data into equation (26).

$$P_1 = f_p(XF_r + YF_a)$$

$$P_1 = 1.2(0.41 \times 1852.86 + 0.87 \times 300)$$

$P_1 = 224.8N$ *Calculation of rated dynamic load*

The dynamic load rating C_r, of the bearing required for AGV operation can be calculated from equation (28)

$$\frac{P}{F_t}\left(\frac{60n}{10^6}L_h\right)^{\frac{1}{\varepsilon}} \tag{28}$$

Where

n is the rotational speed of the shaft, in *"r/min."*

FT is the temperature coefficient.

L_h is the expected calculated life.

εIs the life index, and the life index of the ball bearing is $\varepsilon = 3$.

According to the work content of AGV, the predicted life expectancy is 8000h. The data is put into the formula (30)

$$C_r \ \frac{1224.8}{1}\left(\frac{60\times53}{10^6}8000\right)^{\frac{1}{3}} = 3602.2\ N.m$$

According to the parameters of the 7205ACJ bearing, the rated dynamic load is 12.4 kN, which is much larger than 3.6022.

Therefore, the 7205ACJ bearing is safe in this design.

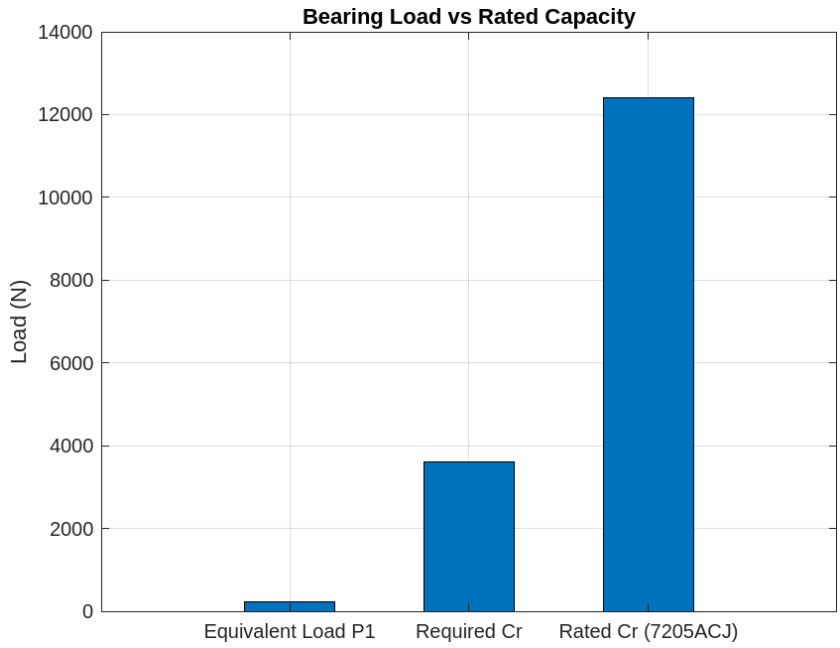

Figure 12. Comparison between the calculated equivalent (P_1), (C_r), and the rated capacity of the bearing

5.4. Key dimensioning and strength verification

In this design, the selected flat key is calculated according to the extrusion stress on the working surface. The strength of the normal level connection should be satisfied with the formula (29).

$$\sigma_p = \frac{2T\times10^3}{dkl} \leq [\sigma_p] \quad (29)$$

Where.

T is the transmitted torque, and the unit is *"N.m" %*.

K is the contact height of the key to the hub of the keyway.

K = 0.5h; in "mm"

L is the working length of the key,

D is the diameter of the shaft,

σ_p Is the allowable extrusion stress of the weakest material among key, shaft, and hub, and the unit is *"MPa"*

You can get.

K = 0.5h = 0.5×7 = 3.5mm

For 45 steels, the allowable extrusion stress σ_p = 100~120MPa

We will take σ_p = 110MPa

At the wheel $\sigma_p = \frac{2\times31.5\times10^3}{22\times3.5\times12} = 68.2MPa < 110MPa$

At the pulley $\sigma_p = \frac{2\times31.5\times10^3}{27\times3.5\times32} = 20.8MPa < 110MPa$

Coupling $\sigma_p = \frac{2\times63\times10^3}{22\times3.5\times20} = 81.8MPa < 110MPa$

Therefore,

The key strength in all three places is meeting a variety of needs.

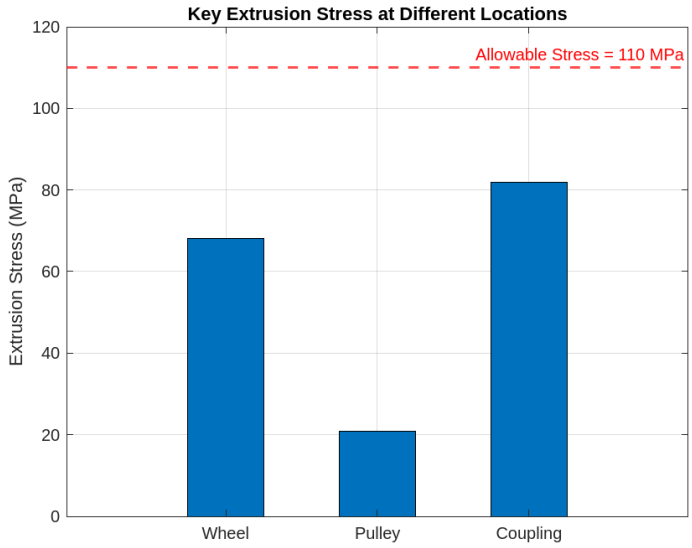

Figure 13. Extrusion stress on the key at the Wheel, Pulley, and Coupling versus allowable limit.

4. Discussion

The developed outdoor Automated Guided Vehicle (AGV) demonstrates significant novelty in combining a lightweight structure (≤70 kg) with a robust dual-motor drive and automatic belt tensioning system. This approach bridges the gap between conventional indoor AGVs and heavy-duty outdoor systems, offering a balance of portability, mechanical efficiency, and terrain adaptability. The integration of two D80-02430B5-E DC servo motors, each with a planetary gear reducer (40:1) provides the necessary torque amplification while maintaining smooth motion control through synchronized belt transmission.

The study's primary contribution lies in the mechanical optimization of the AGV to ensure stable torque distribution, reduced slippage and enhanced operational safety under variable surface conditions. The structural validation through stress analysis confirmed that all shaft and component stresses remained within the allowable limits, demonstrating reliability for extended outdoor use. In the context of existing research, this design advances AGV mobility solutions by introducing a compact dual-drive configuration that minimizes power losses and mechanical wear compared to traditional chain- or hub-driven mechanisms.

The practical implications of this work are substantial for small scale industries warehouse logistics, and smart transportation systems where compact energy-efficient and low-maintenance AGVs are required. However, the study is limited to mechanical design and static validation; dynamic testing under real outdoor environments and integration with navigation or sensor modules were beyond its current scope. Future work should focus on implementing intelligent path-planning, real-time feedback control and autonomous perception systems to further enhance performance and adaptability in complex outdoor conditions.

5. Conclusions

An automated guided vehicle (AGV) is defined as a group of collaborative driverless vehicles, which are used in the production workshop and coordinated by a centralized or distributed computer-based control system. As mentioned above, their main purpose is to facilitate the automated process of manufacturing subjects. This study provides a complete methodology to design outdoor AGVs. The AGV, an automatic guided vehicle, is composed of mechanical parts, sensors, and information processing parts. Through the design, the AGV automatically moves on the pre-set trajectory so that the workpiece is automatically transported in the flexible manufacturing system. The methodology has been applied to a practical case, but it can easily be employed to develop vehicles with different load capacities and sizes. Moreover, the AGV vibrates while moving along the circular path at high speed we can correct it as further work. The structure can allow more connections in FMS by increasing the intelligence system. Future improvements to this AGV may include full integration with navigation and perception systems. Mounting LiDAR, ultrasonic sensors, or vision systems will require structural interfaces and protection from outdoor environmental elements. Additionally, vibrations from mechanical systems may interfere with sensor stability, necessitating shock-absorbing mounts or isolation pads. Other upgrades include real-time feedback control for torque or belt tension, adaptive PID controllers and battery management systems. The design could also be scaled to support modular attachments or multiple payload configurations. Long-term testing across seasons will validate robustness under realistic operational stress.

References:

1. Bhargava, A., Suhaib, M. & Singholi, A.S. A review of recent advances, techniques, and control algorithms for automated guided vehicle systems. J Braz. Soc. Mech. Sci. Eng. 46, 419 (2024). https://doi.org/10.1007/s40430-024-04896-w
2. Y. Zhou et al., "Integrated Sensing, Communication, and Control Driven Multi-AGV Closed-Loop Control," in IEEE Transactions on Vehicular Technology, vol. 74, no. 7, pp. 10853-10868, July 2025, doi: 10.1109/TVT.2025.3546650. N Kumar, A Agrawal, & R Singh. (2024). AGV Control using Voice Command.
3. Siegfried, P. & Arafa, R. (2023). A review of automated guided transport systems: dispatching systems and navigation concepts. Road Transport, (52), 80–88. https://doi.org/10.30977/AT.2219-8342.2023.52.0.09 M. Aizat, A. Azmin, & Wan Rahiman. (2023). A Survey on Navigation Approaches for Automated Guided Vehicle Robots in Dynamic Surrounding. In IEEE Access.
4. Yishuai Lin, Yunlong Xu, Jiawei Zhu, Xuhua Wang, Liang Wang, Gang Hu, MLATSO: A method for task scheduling optimization in multi-load AGVs-based systems, Robotics and Computer-Integrated Manufacturing, Volume 79, 2023, 102397, ISSN 0736-5845, https://doi.org/10.1016/j.rcim.2022.102397.
5. Fan, H., Li, D., Ouyang, B. et al. Improving scheduling in multi-AGV systems by task prediction. J Sched 27, 299–308 (2024). https://doi.org/10.1007/s10951-023-00792-8
6. Wang, G., Zou, Y., Yang, Y. et al. Dynamic Scheduling Based on Two-Layer Deep Reinforcement Learning for Multi-load AGVs. Circuits Syst Signal Process 44, 6445–6466 (2025). https://doi.org/10.1007/s00034-025-03118-5
7. Liu, F., Lu, C., & Li, X. (2024). A History-Guided Regional Partitioning Evolutionary Optimization for Solving the Flexible Job Shop Problem with Limited Multi-load Automated Guided Vehicles. ArXiv. https://arxiv.org/abs/2409.18742
8. Hu, Y., Yang, H., & Huang, Y. (2022). Conflict-free scheduling of large-scale multi-load AGVs in material transportation network. Transportation Research Part E: Logistics and Transportation Review, 158, 102623. https://doi.org/10.1016/j.tre.2022.102623
9. Fedorko, G., Honus, S., & Salai, R. (2017). Comparison of the traditional and autonomous AGV systems. In MATEC Web of Conferences (Vol. 134, p. 00013). EDP Sciences. https://www.matec-conferences.org/articles/matecconf/pdf/2017/48/matecconf_logi2017_00013.pdf
10. Chen, Z. (2024). Analysis of the application scenarios of different sensors in automated guided vehicles. Highlights in Science Engineering and Technology, 114, 122–128. https://pdfs.semanticscholar.org/1f49/c2f5b258e85c3e863545a96d83a348d11ec2.pdf

[1] Article Affiliation
Author email address

11. Bhargava, A., Suhaib, M. & Singholi, A.S. A review of recent advances, techniques, and control algorithms for automated guided vehicle systems. *J Braz. Soc. Mech. Sci. Eng*. **46**, 419 (2024). https://doi.org/10.1007/s40430-024-04896-w
12. Datcu, D., Winkel, J., & Rothkrantz, L. (2022). Augmented reality to support parcel handling in last-mile logistics. Acta Polytechnica CTU Proceedings, 39, 1-5. https://doi.org/10.14311/APP.2022.39.0001
13. W. Liu, "Route Optimization for Last-Mile Distribution of Rural E-Commerce Logistics Based on Ant Colony Optimization," in *IEEE Access*, vol. 8, pp. 12179-12187, 2020, doi: 10.1109/ACCESS.2020.2964328.
14. P. Yee Leong and N. S. Ahmad, "Exploring Autonomous Load-Carrying Mobile Robots in Indoor Settings: A Comprehensive Review," in IEEE Access, vol. 12, pp. 131395-131417, 2024, doi: 10.1109/ACCESS.2024.3435689.
15. Clauer, D., Fottner, J., Rauch, E., & Prüglmeier, M. (2020). Usage of Autonomous Mobile Robots Outdoors - an Axiomatic Design Approach. Procedia CIRP, 96, 242-247. https://doi.org/10.1016/j.procir.2021.01.081
16. Mehta, D., Kosaraju, K.C., and Krovi, V.N., “Actively Articulated Wheeled Architectures for Autonomous Ground Vehicles - Opportunities and Challenges,” SAE Technical Paper 2023-01-0109, 2023, doi:10.4271/2023-01-0109.
17. Dudeja, H., Bagal, L., Zunjur, N., & Jagadale, S. S. (2015). Mechanical design of an automated guided vehicle (AGV). Int. J. Res. Aeronaut. Mech. Eng, 3(5), 32-40. https://www.academia.edu/download/104133494/V3i509.pdf
18. J. Chen, K. Wen, J. Xia, R. Huang, Z. Chen and W. Li, "Knowledge Embedded Autoencoder Network for Harmonic Drive Fault Diagnosis Under Few-Shot Industrial Scenarios," in IEEE Internet of Things Journal, vol. 11, no. 13, pp. 22915-22925, 1 July1, 2024, doi: 10.1109/JIOT.2024.3362343.
19. Xu et al., "Online Knowledge Distillation-Based Multiscale Threshold Denoising Networks for Fault Diagnosis of Transmission Systems," in IEEE Transactions on Transportation Electrification, vol. 10, no. 2, pp. 4421-4431, June 2024, doi: 10.1109/TTE.2023.3313986.
20. X. Lei, G. Zhang, S. Li, H. Qian and Y. Xu, "Dual-spring AGV shock absorption system design: Dynamic analysis and simulations," 2017 IEEE International Conference on Robotics and Biomimetics (ROBIO), Macau, Macao, 2017, pp. 1068-1074, doi: 10.1109/ROBIO.2017.8324559.
21. Mu, H. (2023). Analysis and Discussion on Tension of Long Transport Belt. In MATEC Web of Conferences (Vol. 380, p. 01024). EDP Sciences. https://doi.org/10.1051/matecconf/202338001024
22. L. Jin, X. Zhu, J. Huan, C. Li and X. Duan, "Passive Gravity Compensation for Parallel Mechanism With Both Spatial Translations and Angular Orientations," in IEEE Robotics and Automation Letters, vol. 9, no. 3, pp. 2279-2286, March 2024, doi: 10.1109/LRA.2024.3355734.
23. Wang, L., Feng, Q., Huang, W., Hu, B., & Su, L. (2017). DIFFERENTIAL DRIVE AND STEERING CONTROL TECHNOLOGY OF AUTOMATIC NAVIGATION HANDLING TOOL BASED ON PLC. International Journal of Mechatronics and Applied Mechanics, 2, 134-138. https://ijomam.com/wp-

content/uploads/2017/12/134-138_DIFFERENTIAL-DRIVE-AND-STEERING-CONTROL-TECHNOLOGY-OF-AUTOMATIC-NAVIGATION.pdf

24. Hlaing, T. T., Nwet, T. T., & Myat, S. (2019). Overview of Differences between Servo and Stepper Motor Technology. Internatiojnal Journal of Advanced Engineering and Science, 4(3), 169-171. http://irjaes.com/wp-content/uploads/2020/10/IRJAES-V4N3P86Y19.pdf
25. Akash, R. K. (2025). Comparative Analysis of Control Strategies for Position Regulation in DC Servo Motors. ArXiv. https://arxiv.org/abs/2501.11820
26. Hlaing, T. T., Nwet, T. T., & Myat, S. (2019). Overview of Differences between Servo and Stepper Motor Technology. Internatiojnal Journal of Advanced Engineering and Science, 4(3), 169-171. http://irjaes.com/wp-content/uploads/2020/10/IRJAES-V4N3P86Y19.pdf
27. Honkalas, R., Deshmukh, B., & Pawar, P. (2021, July). A review on design and efficiency improvement of worm and worm wheel of a gear motor. In Journal of Physics: Conference Series (Vol. 1969, No. 1, p. 012023). IOP Publishing. https://iopscience.iop.org/article/10.1088/1742-6596/1969/1/012023/pdf
28. Irakoze, V., Ceccarelli, M., Russo, M. (2022). Historical and Technical Analysis of Harmonic Drive Gear Design. In: Pucheta, M., Cardona, A., Preidikman, S., Hecker, R. (eds) Multibody Mechatronic Systems. MuSMe 2021. Mechanisms and Machine Science, vol 110. Springer, Cham. https://doi.org/10.1007/978-3-030-88751-3_5
29. Ibragimov, O.D., Saksonov, A.S. & Kozlovskii, V.N. Stages of Development and Current Trends in the Development and Production of Automobile Electric Gear Motors. *Russ. Engin. Res.* 44, 579–583 (2024). https://doi.org/10.3103/S1068798X24700448
30. Arnaudov, K., & Karaivanov, D.P. (2019). Planetary Gear Trains (1st ed.). CRC Press. https://doi.org/10.1201/9780429458521
31. J. F. Kayode, J. O. Akinyoola, T. Ogedengbe, A. A. Noiki, S. A. Afolalu and A. O. Akinola, "Design and Optimization of a Flange Coupling using Finite Element Analysis," *2024 International Conference on Science, Engineering and Business for Driving Sustainable Development Goals (SEB4SDG)*, Omu-Aran, Nigeria, 2024, pp. 1-8, doi: 10.1109/SEB4SDG60871.2024.10629818.
32. Patel, N. R., Paskanthi, M., Makwana, I., Hotchandani, P., & Vasava, S. (2020). Comparative analysis of resilient grid coupling by analytical design. Int. J. Res. Appl. Sci. Eng. Technol, 8(11). http://doi.org/10.22214/ijraset.2020.2008
33. Yao, Y., Cao, W., & Li, Q. (2019). Discussion on the Prediction Method of the Running Resistance of Tracked Vehicle. https://webofproceedings.org/proceedings_series/ESSP/ICISS%202019/ICISS19070.pdf
34. M. Boehning, "Improving safety and efficiency of AGVs at warehouse black spots," 2014 IEEE 10th International Conference on Intelligent Computer Communication and Processing (ICCP), Cluj-Napoca, Cluj, Romania, 2014, pp. 245-249, doi: 10.1109/ICCP.2014.6937004.
35. Sebesan, I., & Tarus, B. (2012). Experimental determinations of the aerodynamic drag for vehicles subjected to the ground effect. INCAS Bulletin, 4(2), 99. DOI: 10.13111/2066-8201.2012.4.2.11

36. J. Leng, J. Peng, J. Liu, Y. Zhang, J. Ji and Y. Zhang, "Profiling Power Consumption in Low-Speed Autonomous Guided Vehicles," in IEEE Robotics and Automation Letters, vol. 9, no. 7, pp. 6027-6034, July 2024, doi: 10.1109/LRA.2024.3396051.
37. TANG, H. J., SHI, S. J., HUANG, P. L., WANG, D., & ZHOU, J. (2018). PID control of magnetic navigation differential AGV trajectory. DEStech Trans. Eng. Technol. Res, (apop), 500-506. https://scholar.archive.org/work/2a6tqpl7lbgknn7try5cvajmhe/access/wayback/http://dpi-proceedings.com/index.php/dtetr/article/download/18774/18270
38. Guo, J. H., Jiang, H. Y., Wu, Y. Z., Chu, W. Y., & Meng, Q. X. (2014, August). Double helical synchronous belt transmission design. In Materials Science Forum (Vol. 800, pp. 672-677). Trans Tech Publications Ltd. https://doi.org/10.4028/www.scientific.net/MSF.800-801.672
39. Shi, Yaochen, Zhanguo Li, and Yan Li. "The Study of Synchronous Belt Transmission Stability with the Influence of Rotation Speed and Tension." *International Journal of Smart Home* 9.10 (2015): 145-152. http://dx.doi.org/10.14257/ijsh.2015.9.10.16
40. Önnered, S. (2020). Automatic Belt Tension Device. https://lup.lub.lu.se/luur/download?func=downloadFile&recordOId=9022902&fileOId=9022903
41. Pradhan, M. N., & Gaikwad, H. T. (2015). Fatigue analysis of composite drive shaft. International Journal of Engineering Research and Technology, 4(5), 484-489. https://www.academia.edu/download/64200536/fatigue-analysis-of-composite-drive-shaft-IJERTV4IS050628.pdf
42. Barykin, A.Y., Mukhametdinov, M.M., Takhaviev, R.K. (2022). Drive Axle of Vehicle and Environment Impact. In: Radionov, A.A., Gasiyarov, V.R. (eds) Proceedings of the 7th International Conference on Industrial Engineering (ICIE 2021). ICIE 2021. Lecture Notes in Mechanical Engineering. Springer, Cham. https://doi.org/10.1007/978-3-030-85233-7_77
43. Funing Xu, Ning Ding, Nan Li, Long Liu, Nan Hou, Na Xu, Weimin Guo, Linan Tian, Huixia Xu, Chi-Man Lawrence Wu, Xiaofeng Wu, Xiangfeng Chen, A review of bearing failure Modes, mechanisms and causes, Engineering Failure Analysis, Volume 152, 2023, 107518, ISSN 1350-6307, https://doi.org/10.1016/j.engfailanal.2023.107518.
44. Jacobs, W., Boonen, R., Sas, P., & Moens, D. (2012, May). The effect of external dynamic loads on the lifetime of rolling element bearings: accurate measurement of the bearing behaviour. In Journal of Physics: Conference Series (Vol. 364, No. 1, p. 012037). IOP Publishing. DOI: 10.1088/1742-6596/364/1/012037
45. Salunkhe, Vishal G., Ramchandra Ganapati Desavale, and Surajkumar G. Kumbhar. "Vibration analysis of deep groove ball bearing using finite element analysis and dimension analysis." *Journal of Tribology* 144.8 (2022): 081202. https://doi.org/10.1115/1.4053262
46. Koroliov, A., Kozlov, I., Pavlyshyn, P., Turmanidze, R., Yeputatov, Y. (2021). Device for Electric Drives Torque Diagnostics and Its Characteristics Study. In: Tonkonogyi, V., *et al.* Advanced Manufacturing Processes II . InterPartner 2020. Lecture Notes in Mechanical Engineering. Springer, Cham. https://doi.org/10.1007/978-3-030-68014-5_16

47. P. Zhang, Y. Ding and Y. Chen, "Obstacle Avoidance Control of the AGV With Actuator Dead Zones Based on Fixed-Time Disturbance Observers and Command Filtering," in IEEE Access, vol. 12, pp. 66701-66716, 2024, doi: 10.1109/ACCESS.2024.3398352.
48. B. Yu, Y. Zhang, L. Zhang and P. Jia, "AGV Structure Design for Transporting Photovoltaic Panels," 2023 7th International Conference on Electrical, Mechanical and Computer Engineering (ICEMCE), Xi'an, China, 2023, pp. 244-248, doi: 10.1109/ICEMCE60359.2023.10490637.
49. M. R. Imani et al., "Dynamic Analysis of Forklift AGV based on Center of Gravity," 2024 International Electronics Symposium (IES), Denpasar, Indonesia, 2024, pp. 322-328, doi: 10.1109/IES63037.2024.10665882.
50. K. Osman, J. Ghommam and M. Saad, "Combined road following control and automatic lane keeping for automated guided vehicles," 2016 14th International Conference on Control, Automation, Robotics and Vision (ICARCV), Phuket, Thailand, 2016, pp. 1-6, doi: 10.1109/ICARCV.2016.7838680.
51. Bayona, E., Sierra-García, J. E., & Peñas, M. S. (2025). Improving Safety and Efficiency of Industrial Vehicles by Bio-Inspired Algorithms. Expert Systems, 42(3), e13836. https://doi.org/10.1111/exsy.13836